

accommodate story-drift (i.e., inter-story lateral displacement divided by story height) of nearly 1% without significant damage and about 2% with damage but without failure (Kurama et al. 1999).

The extremely narrow hysteresis loops in Fig. 2 indicate that the inelastic energy dissipation of the wall is very small. Fig. 3 shows a comparison between the roof-drift time-histories of Wall WH1 (solid line) and a comparable monolithic cast-in-place reinforced concrete wall (dashed line) from nonlinear dynamic time-history analyses under the Hollister ground motion (recorded during the 1989 Loma Prieta earthquake) scaled to a peak acceleration of 0.52g. The walls have the same strength, initial stiffness, drift capacity, initial fundamental period, and viscous damping. Thus, the only difference between the walls is their hysteretic behavior under lateral load (Kurama et al. 1999). The inelastic energy dissipation of the cast-in-place wall is approximately twice the inelastic energy dissipation of Wall WH1, however the cast-in-place wall has a very small self-centering capability.

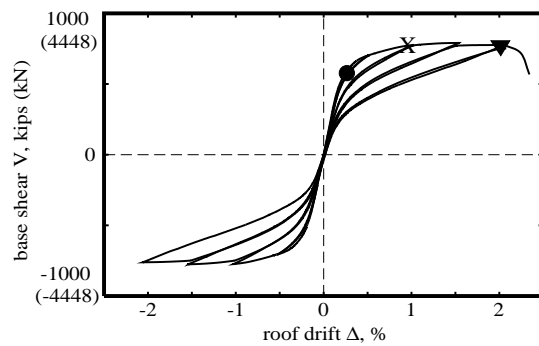


Figure 2. Hysteretic behavior under lateral load

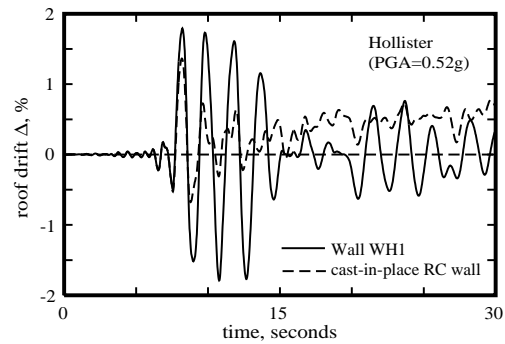


Figure 3. Roof-drift time-history

Three important differences are observed between the two walls in Fig. 3: (1) the maximum roof-drift of Wall WH1 is larger; (2) the response of Wall WH1 decays less rapidly resulting in a large number of large drift cycles; and (3) Wall WH1 oscillates around the zero-drift position, whereas, the cast-in-place wall accumulates a residual drift (residual roof-drift $\approx 0.5\%$) indicating significant damage.

A series of nonlinear dynamic time-history analyses using fifteen ground motions indicate that the maximum roof-drift of unbonded post-tensioned precast walls can be, on average, 40% larger than the maximum roof-drift of comparable monolithic cast-in-place concrete walls (Kurama et al. 1997, 1999). These displacements can be reduced by using supplemental passive energy dissipation as described in this paper. Passive energy dissipation systems may require up to 1% story-drift in order to have the damper deformations that are needed to dissipate sufficient energy. Properly-designed unbonded post-tensioned precast walls can accommodate these deformations without significant damage.

2. BEHAVIOR UNDER LATERAL LOAD

This section gives background information on the behavior of unbonded post-tensioned precast walls under combined lateral loads and gravity loads. More detailed information on this topic can be found in Kurama et al. (1997, 1999). Fig. 4 shows the base-shear-roof-drift relationship of Wall WH1 from a nonlinear static push-over analysis. As the wall displaces, it goes through four states.

1. The *decompression state* (indicated by a ■ marker at a base shear and roof-drift of V_{dec} and Δ_{dec}) identifies the initiation of a gap opening along the horizontal joint between the wall and the foundation.

2. The *softening state* (indicated by a ● marker at V_{e11} and Δ_{e11}) identifies the beginning of a significant reduction in the lateral stiffness of the wall due to gap opening along the horizontal joints and a small amount of nonlinear behavior of the concrete in compression.

3. The *yielding state* (indicated by a X marker at V_{lp} and Δ_{lp}) identifies the point at which the strain in the post-tensioning steel first reaches the limit of proportionality. Because of unbonding of

the post-tensioning steel, a properly-designed wall does not reach the yielding state until a large nonlinear drift has occurred. Up to the yielding state, noticeable damage to the concrete in compression other than spalling of the cover concrete over a small region near the base of the wall is small because the spiral reinforcement provides heavy confinement. Damage in the wall due to cracking is also small because the post-tensioning steel does not transfer significant tensile stresses into the concrete due to unbonding. The yielding state for Wall WH1 is reached at approximately 0.84% roof-drift

(Fig. 4), which corresponds to 0.96% story-drift in the top (sixth) story and 0.57% story-drift in the bottom story. Thus, the wall can accommodate up to 0.96% story-drift without significant damage.

4. The *failure state* (indicated by a ▼ marker at V_{csc} and Δ_{csc}) identifies axial-flexural failure of the wall which occurs as a result of crushing of the spiral confined concrete. Crushing of the spiral confined concrete occurs when the spiral reinforcement fractures. Sufficient spiral reinforcement is provided in the wall such that the failure state is reached at a drift significantly larger than the drift at the yielding state. The failure state for Wall WH1 is reached at approximately 2.0% roof-drift, which corresponds to 2.2% story-drift in the top story and 1.7% story-drift in the bottom story. Thus, the wall can accommodate up to 2.2% story-drift without failure.

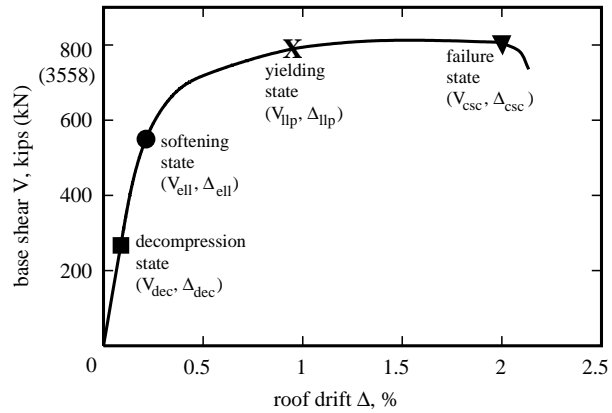


Figure 4. Base-shear-roof-drift relationship

3. PROPOSED SUPPLEMENTAL PASSIVE ENERGY DISSIPATION SYSTEM

The proposed supplemental energy dissipation system is shown in Fig. 5. Linear viscous-fluid dampers are used in brace elements placed diagonally in-plane with the wall. The brace elements which support the dampers are anchored to the wall at one end, and to a column (referred to as the bracing column) at the other end. The bracing columns are designed to displace laterally with the wall and to resist the damper forces. The design of the bracing columns is not discussed in the paper.

The proposed system uses the gap opening displacements that occur along the horizontal joints as shown in Fig. 6. Fig. 7 shows the damper deformations that occur in Wall WH1 at the yielding state for the damper configuration shown in Fig. 5. The dampers are placed at approximately 45 degrees with the horizontal. The results indicate that damper deformations of up to 1.8 in (4.6 cm) can be achieved without significant damage in the wall.

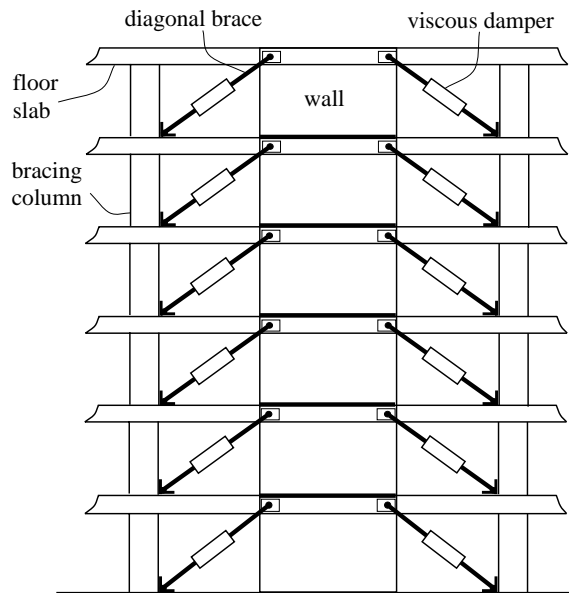


Figure 5. Proposed supplemental energy dissipation system

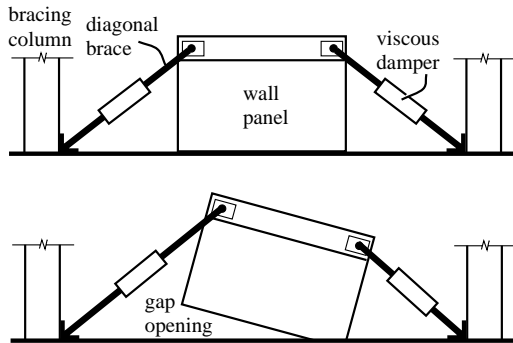


Figure 6. Damper deformation

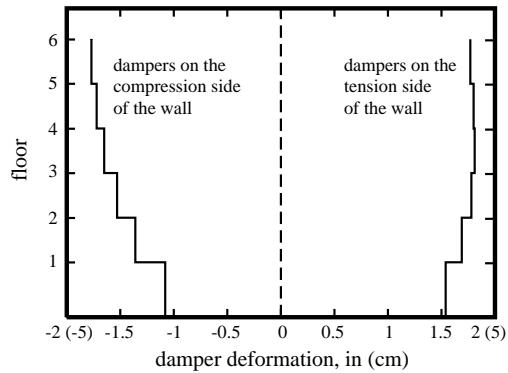


Figure 7. Damper deformation in Wall WH1 at Δ_{lp}

3.1. Analytical Modeling

An analytical model of Wall WH1 with the supplemental energy dissipation system shown in Fig. 5 was developed to conduct nonlinear static and dynamic analyses. The wall was modeled using fiber beam-column elements as described by Kurama et al. (1997, 1999). A significant advantage of using fiber beam-column elements for the wall is that a reasonably accurate model can be developed using only uniaxial stress-strain models for concrete and post-tensioning steel and the dimensions of the wall. The model accounts for axial-flexural interaction, hysteretic behavior of the post-tensioning steel and concrete including crushing of concrete, and gap opening along the horizontal joints.

The linear viscous-fluid dampers were modeled using truss elements. The damping constant, C of the dampers was modeled as $C = \beta k$ using stiffness proportional damping, where β is the stiffness proportionality factor and k is the stiffness under static loading. A “large” value of β and a “small” value of k were used for the truss elements such that the initial stiffness of the wall under static lateral loads was not significantly affected by the truss elements modeling the dampers. In the analytical model for Wall WH1, the initial stiffness increased by approximately 2% due to the truss elements.

The flexibility of the diagonal bracing elements was ignored. The bracing columns were assumed to displace laterally the same amount with the wall (assuming a rigid floor system). The axial deformation of the bracing columns was ignored.

4. PROPOSED DESIGN APPROACH

This section describes a proposed seismic design approach for the supplemental energy dissipation system shown in Fig. 5. In this design approach, the capacity of the structure in the form of a generalized “capacity curve” is compared with equivalent seismic demands in the form of ground motion “demand spectra” as described below using Fig. 8.

4.1. Ground Motion Demand Spectra

The demand spectra for a ground motion are constructed by plotting the linear-elastic single-degree-of-freedom (SDOF) pseudo-acceleration response spectra, S_a versus the displacement response spectra, S_d for different values of coefficient of viscous damping, ξ . In the design of the supplemental energy dissipation system for Wall WH1, average demand spectra using seven ground motions for sites with a medium soil profile were used. These ground motions include five selected natural ground motions and two artificial ground motions as shown in Table 1.

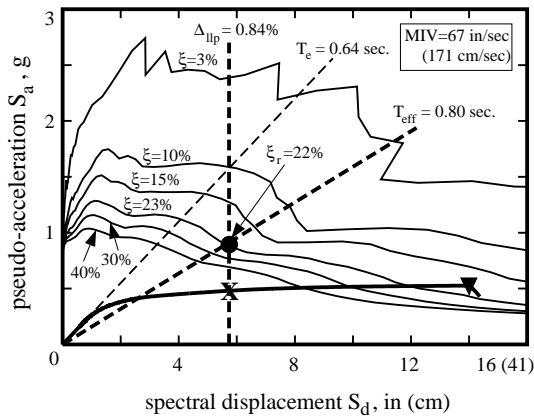


Figure 8. Proposed design approach

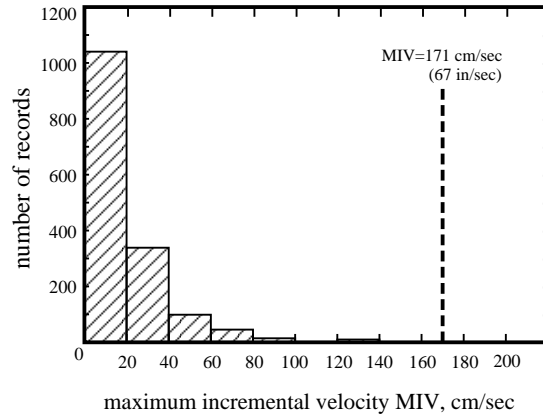


Figure 9. Maximum incremental velocity

In order to represent a uniform level of seismic intensity for Wall WH1, the ground motions were scaled to a constant maximum incremental velocity (MIV). The MIV of a ground motion is the maximum area under the acceleration time-history of the ground motion between two zero crossings. Nonlinear dynamic time-history analyses of Wall WH1 without supplemental energy dissipation indicate that the drift is strongly correlated with MIV (Kurama et al. 1997).

The ground motions were scaled to MIV=67 in/sec. (171 cm/sec.) which is approximately equal to the MIV of the generated (Kurama et al. 1997) design spectrum compatible ground motion (G1M) scaled to a peak acceleration of 1.0g. Fig. 9 shows the MIV of 1545 ground motions recorded in North America and Hawaii between 1933-1992 (adapted from Naeim and Anderson 1993). The MIV=171 cm/sec. value of the scaled ground motions is larger than the MIV of the 1545 recorded ground motions. Similarly, the largest MIV recorded during the 1994 Northridge earthquake is 152 cm/sec. (at the Newhall station) which is close to but smaller than the MIV=171 cm/sec. value used in scaling. Thus, the MIV-scaled ground motions in Table 1 are considered to be representative of maximum credible ground motions that can be expected in the regions of the U.S. with high seismicity.

Table 1 shows the peak acceleration (PGA), peak velocity (PGV), maximum incremental velocity (MIV), effective peak acceleration (EPA), and effective peak velocity (EPV) of the MIV-scaled ground motions. The EPA was calculated as the average linear-elastic SDOF spectral pseudo-acceleration (for $\xi=5\%$) for periods between 0.1-0.5 sec. divided by 2.5, and the EPV was calculated as the average linear-elastic SDOF spectral pseudo-velocity (for $\xi=5\%$) for periods between 0.8-1.2 sec. divided by 2.5. In Table 1, the ground motions are listed in the order of increasing PGA.

Table 1. The MIV-scaled ground motion records

Earthquake	Recording station or method of generation	Soil profile	PGA (g)	PGV (in/sec.)	MIV (in/sec.)	EPA (g)	EPV (in/sec.)
Loma Prieta, 1989	Hollister-South and Pine	medium	0.52	35	67	0.32	31
Landers, 1992	Yermo-Fire Station		0.62	51	67	0.43	27
Northridge, 1994	Newhall-LA County Fire St.		0.66	42	67	0.61	32
San Fernando, 1971	LA 8244 Orion Bl. 1 st floor		0.95	44	67	0.82	29
Northridge, 1994	Sylmar-County Hosp. Park.		0.97	58	67	0.82	25
G1M-generated	Design Spectrum Compatible		1.0	107	67	0.98	38
G2M-generated	Using Kanai-Tajimi Filter		1.1	112	67	1.0	33

The average demand spectra for the MIV-scaled ground motions for damping ratios of $\xi = 3\%$, 10% , 15% , 23% , 30% , and 40% are shown by the solid lines in Fig. 8. The radial lines correspond to lines of constant period which increase in the clockwise direction ($S_a/S_d = \omega^2 = 4\pi^2/T^2$).

4.2. Structure Capacity Curve

The capacity curve of Wall WH1 was determined from the base-shear-roof-drift relationship shown in Fig. 4. For this purpose, the base shear, V and roof-drift, Δ were converted to the acceleration, G_a and displacement, G_d of a generalized SDOF system, respectively. The generalized acceleration was calculated as $G_a = V/(L\Gamma)$ and the generalized displacement was calculated as $G_d = \Delta/\Gamma$, where, $L = \{\phi_1\}^T [M] \{1\}$, $\Gamma = L/M^*$, $M^* = \{\phi_1\}^T [M] \{\phi_1\}$, $\{\phi_1\}$ = linear-elastic fundamental mode shape normalized with respect to the roof, and $[M]$ = mass matrix.

The generalized capacity curve for Wall WH1 is plotted with the average demand spectra in Fig. 8 to compare equivalent structure capacities with equivalent seismic demands. The heavy solid line is the generalized capacity curve calculated using $L = 3.06 \text{ kip}\cdot\text{sec}^2/\text{in}$ ($5.36 \text{ kN}\cdot\text{sec}^2/\text{cm}$) and $\Gamma = 1.43$ for Wall WH1. Both S_a and G_a are normalized with respect to g . The light radial line corresponds to the linear-elastic fundamental period of the structure, $T_e = 0.64 \text{ sec}$.

4.3. Required Damping

The generalized capacity curve and the average demand spectra were used to estimate the required viscous damping ratio, ξ_r to reduce the maximum roof-drift to a target roof-drift as described below. A target roof-drift of Δ_{lp} (corresponding to the yielding state) was selected to prevent significant damage in Wall WH1.

The vertical line in Fig. 8 corresponds to the target roof-drift of $\Delta_{lp} = 0.84\%$ converted to the generalized displacement as described above. The heavy radial line corresponds to an “effective” fundamental period for the structure which was estimated as follows.

The effective fundamental period, T_{eff} represents an elongation in the fundamental period of the structure due to the nonlinear behavior that occurs when Δ_{lp} is reached. In order to obtain an estimate for T_{eff} , a series of nonlinear dynamic time-history analyses of Wall WH1 were conducted using broadband excitation with increasing intensity. For each intensity of the broadband excitation, the maximum roof-drift and the predominant fundamental period of the structure were obtained. The predominant fundamental period was determined from the phase angle of the transfer function for the roof-drift response. The resulting relationship between the maximum roof-drift and the predominant period was used to estimate T_{eff} as shown in Fig. 10. Corresponding to $\Delta_{lp} = 0.84\%$, $T_{eff} = 0.80 \text{ sec}$. was estimated representing a 25% elongation over the initial linear-elastic period, $T_e = 0.64 \text{ sec}$.

The intersection point between the vertical line (at $\Delta_{lp} = 0.84\%$) and the heavy radial line (at $T_{eff} = 0.80 \text{ sec}$.) in Fig. 8 was used to estimate the required viscous damping ratio to achieve the target roof-drift, ξ_r . As shown in Fig. 8, the estimated ξ_r is 22%. The damping constant, C of the dampers to achieve $\xi_r = 22\%$ was determined from a linear-elastic modal analysis of the wall with the supplemental energy dissipation system. It was assumed that the system without supplemental energy dissipation has a viscous damping ratio of 3% in the first and the third modes (using Rayleigh damping). The estimated damper constant for the damper arrangement in Fig. 5 is $C = 14.7 \text{ kip}\cdot\text{sec}/\text{in}$ ($25.7 \text{ kN}\cdot\text{sec}/\text{cm}$).

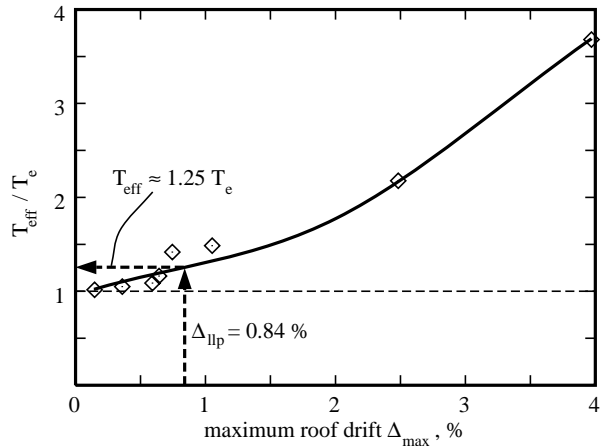


Figure 10. Estimation of T_{eff}

5. EVALUATION OF DYNAMIC RESPONSE

In this section, the proposed supplemental energy dissipation system and the design approach are evaluated based on nonlinear dynamic time-history analyses of Wall WH1. The wall with supplemental energy dissipation is referred to as the damped wall and the wall without supplemental energy dissipation is referred to as the undamped wall. The dynamic analyses were conducted using the MIV-scaled ground motions in Table 1 and with a time step of 0.01 sec.

Fig. 11 shows the maximum roof-drift obtained from the dynamic analyses of the damped wall and the undamped wall. The dashed horizontal line represents the target roof-drift, $\Delta_{lp}=0.84\%$. The results indicate that the supplemental energy dissipation system and the design approach are effective in reducing the maximum roof-drift to the target roof-drift. The average maximum roof-drift for the damped wall is 0.86% which is very close to the target roof-drift of 0.84%. The average maximum roof-drift for the undamped wall is 2.4%. On average, the ratio between the maximum roof-drift of the damped wall and the undamped wall is equal to 0.37.

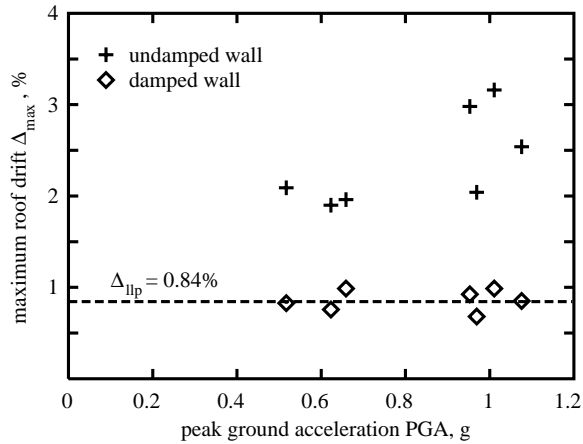


Figure 11. Maximum roof drift

Fig. 12 shows a comparison between the roof-drift time-history of the damped wall and the undamped wall under the MIV-scaled San Fernando-Orion and Northridge-Newhall ground motions. The dashed horizontal line represents the target roof-drift. The time-history results indicate that the supplemental energy dissipation system is effective in reducing the large roof-drift cycles that occur in the undamped wall after the maximum roof-drift is reached.

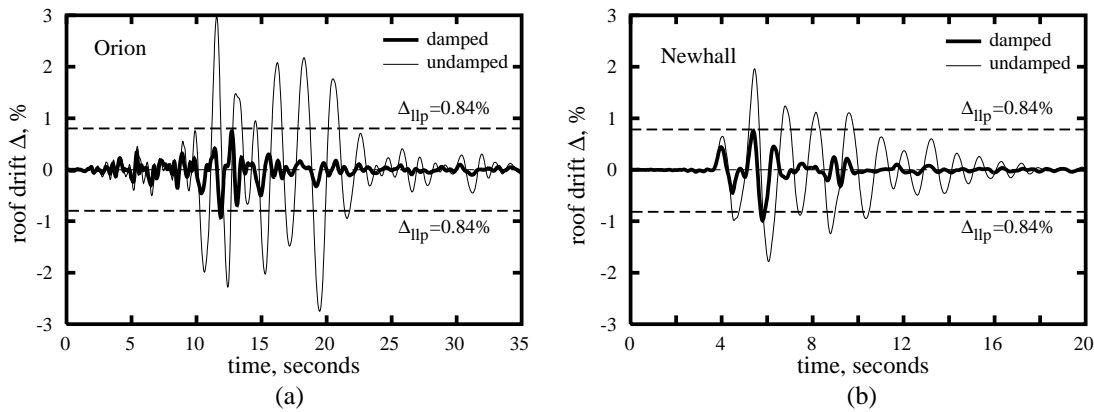


Figure 12. Roof-drift time-history: (a) Orion ground motion; (b) Newhall ground motion

Fig 11 shows that the maximum roof-drift of the damped wall is nearly constant for the seven MIV-scaled ground motions indicating that scaling the ground motions to a constant MIV results in a uniform level of seismic intensity for Wall WH1 as discussed in Section 4.1. Table 1 shows that the EPV values of the MIV-scaled ground motions is nearly constant. Thus, scaling of the ground motions to a constant EPV would also result in a nearly constant maximum roof-drift for the damped wall, thus in a uniform level of seismic intensity for Wall WH1.

The dynamic analysis results indicate that the average maximum roof acceleration of the damped wall and the undamped wall is equal to 1.31g and 1.62g, respectively. On average, the ratio between the maximum roof acceleration of the damped wall and the undamped wall is equal to 0.82.

5.1. Dynamic Response of the Dampers

Fig. 13 shows the hysteretic load-deformation response of the two dampers in the top story of Wall WH1 (where the maximum damper forces occur) during the MIV-scaled San Fernando-Orion ground motion. The solid and dashed lines show the response of the dampers on the left and right of the wall, respectively. The maximum force developed in the dampers is 273 kips (1214 kN), the maximum damper deformation is 2.0 in (5.1 cm), and the maximum damper velocity is $273/14.7=18.6$ in/sec. (47.2 cm/sec.). These values are within practically achievable limits.

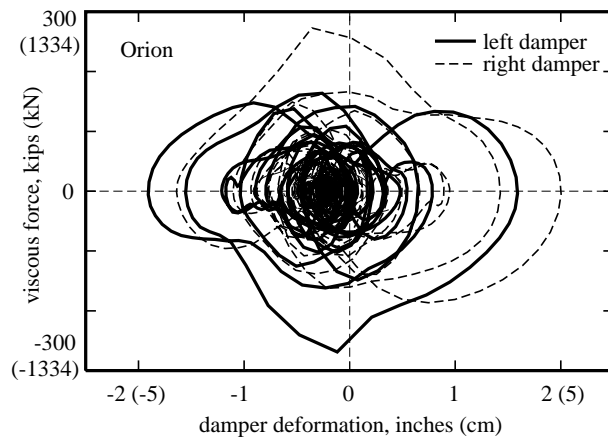


Figure 13. Damper forces

6. CONCLUSIONS

The paper proposes a supplemental passive energy dissipation system for unbonded post-tensioned precast walls using linear viscous-fluid dampers. The energy dissipation system utilizes the nonlinear lateral drift that occurs in the walls due to gap opening along the horizontal joints. A design approach for the proposed supplemental energy dissipation system is introduced.

Nonlinear dynamic time-history analyses of undamped and damped walls show that the proposed supplemental energy dissipation system and the design approach are effective in reducing the maximum roof-drift to a target roof-drift to prevent significant damage in the walls.

ACKNOWLEDGMENTS

The author thanks Professor Billie F. Spencer, Jr. of the University of Notre Dame and Professor Richard Sause of Lehigh University for their comments and suggestions. The opinions, findings, and conclusions expressed in the paper are those of the author and do not necessarily reflect the views of the individuals and organizations acknowledged above.

REFERENCES

- Kurama, Y., Sause, R., Pessiki, S., Lu, L.-W., and El-Sheikh, M. (1997) Seismic Design and Response Evaluation of Unbonded Post-Tensioned Precast Concrete Walls. Research Report No. EQ-97-01, Department of Civil and Environmental Engineering, Lehigh University, Bethlehem, PA 18015, 184 pp.
- Kurama, Y., Pessiki, S., Sause, R., and Lu, L.-W. (1999) Seismic Behavior and Design of Unbonded Post-Tensioned Precast Concrete Walls. *PCI Journal*, Vol. 44, No. 3.
- Naeim, F. and Anderson, J. (1993) Classification and Evaluation of Earthquake Records for Design. The 1993 NEHRP Professional Fellowship Report, EERI.